Article

Not peer-reviewed version

# Experimental Guide for Compact Bow-Tie Femtosecond Solid-State Laser Development

Vinícius Pereira Pinto * , Giovana Trevisan Nogueira , Fátima Maria Mitsue Yasuoka ,
Jarbas Caiado de Castro Neto

Posted Date: 7 January 2025

doi: 10.20944/preprints202501.0318.v1

Keywords: bow-tie configuration; kerr lens mode-locking; high repetition rate laser; low-energy femtosecond laser; compact femtosecond laser

Preprints.org (www.preprints.org) | NOT PEER-REVIEWED | Posted: 7 January 2025 doi:10.20944/preprints202501.0318.v1

*Article*

# Experimental Guide for Compact Bow-Tie Femtosecond Solid-State Laser Development

**Vinícius Pereira Pinto [1,*], Giovana Trevisan Nogueira [2], Fátima Maria Mitsue Yasuoka [1,3] and Jarbas Caiado de Castro Neto [1]**

[1] São Carlos Institute of Physics, University of São Paulo PO BOX 369, São Carlos 13560-970, SP, Brazil
[2] Federal University of Juiz de Fora José Lourenço Kelmer St., Juiz de Fora 36036900, MG, Brazil
[3] BR Labs Tecnologia Óptica e Fotônica Ltda Juan Lopes St., 222 - Jardim São João Batista, São Carlos 13567-020, SP, Brazil
* Correspondence: viniciusppinto@usp.br

**Abstract:** Bow-tie cavity configurations have gained significant attention due to their efficacy in facilitating stable resonator operation for applications requiring short pulse operation and high repetition rate pulses, offering versatility and reliability. While there is an extensive body of literature addressing the theoretical aspects and applications of this laser configuration, there exists a gap in practical insights and systematic approaches guidance pertaining to development and precision alignment of this laser type. The paper achieves this by compiling a range of analytical and optimization techniques for the bow-tie cavity configuration and delineating the necessary steps for optimization required for continuous wave operation. This ultimately leads to the attainment of the pulsed regime through the Kerr Lens Mode-locking technique, offering a detailed account of the development, optimization, and performance evaluation of a Ti:Sapphire femtosecond laser cavity, using dispersion-compensating mirrors to produce a low-energy pulse of 1 nJ, a high repetition rate of 1 GHz, and a short pulse duration of 61 fs. This work can be useful for researchers and engineers seeking to embark on the development of compact and high-performance femtosecond lasers for a spectrum of applications, encompassing biomedical imaging, laser-assisted surgery, spectroscopy, and optical frequency combs.

**Keywords:** bow-tie configuration; kerr lens mode-locking; high repetition rate laser; low-energy femtosecond laser; compact femtosecond laser

## 1. Introduction

The ultrashort pulse generation technology based on Ti:Sapphire laser was first developed in 1986 and has several architecture variations, one of which is the bow-tie configuration [1,2]. This laser type allows efficient and stable laser operation with high tuning and short pulse duration, making it widely regarded as one of the most versatile and reliable options for a variety of applications. At present, many of these applications are well known in a variety of fields, from fundamental scientific research to industrial manufacturing.

There is an abundance of literature on theoretical treatment and applications of this laser type, in which existing studies focus on dispersion compensation [3,4], astigmatism compensation [5,6], thermal effects [7,8], stability regions [9–11], and cavity variations [12–14]. However, there is a gap in the literature regarding optimization studies applied to a cavity, as well as a lack of detailed explanations of the development process. Also, many articles have showcased stability curves and kerr-lens sensitivity curves [15–22], highlighting the theoretical discussion of decreasing the laser confocal parameter. Thus, in practice, this parameter is achieved by fixing one of the mirrors, resulting in a delicate stability region and prolonged working time. This article aims to fill this gap by presenting a compilation of optimization studies and a demonstration of the reproducible development process, with the goal of enabling new technicians and researchers to implement this laser type in significantly shorter time-frames.

doi:10.20944/preprints202501.0318.v1

In this review, the development of a compact benchtop cavity capable of generating ultrafast laser pulses with low pulse energy and high repetition rate is presented, utilizing a minimal number of optical elements. The fundamental principles of femtosecond lasers are first elucidated in a comprehensive and well-referenced manner. Subsequently, the analysis focuses on a simplified bow-tie configuration for Kerr lens mode-locked (KLM) operations, accompanied by correction calculations. An in-depth examination of cavity modes for both continuous-wave (CW) and mode-locked (ML) operations is provided, including the necessary correction calculations. The experimental setup is then meticulously described, with a particular emphasis on critical details essential for cavity alignment and stabilization. This precision is paramount for achieving optimal laser performance and superior pulse quality. It is worth noting that the methodology outlined in this study extends beyond Ti:Sapphire cavities. It can be effectively adapted to replicate similar cavities with variations in specific optical elements or in the solid-state gain medium. This adaptability is particularly relevant in light of recent advancements in Kerr lens mode-locked (KLM) Yb-based diode-pumped solid-state lasers (Yb-DPSSLs) [23].

It is possible to develop lasers with a high repetition rate of more than 1 GHz by combining a compact design with ring cavities, whose repetition rate is twice as high as linear architectures. Thus it is possible to generate high precision frequency combs, which are used in a range of fields, including telecommunications, spectroscopy, and metrology [24–26]. There are also femtosecond laser applications with a high repetition rate in thin film nanomachining [27] and there are articles that show potential in nanomedicine, nanobiotechnology and imaging [28–30] since high repetition rates provide low-energy pulse of about a few nanojoules.

## 2. Overview of Solid-State Lasers Principles

In a laser, an optical cavity houses a gain medium where a beam undergoes amplification and feedback. The gain medium's spectral distribution depends on the type of broadening, which is characterized by a gain coefficient. Laser stability requires that, after completing a round trip in the cavity, the field reproduces geometrically in both phase and amplitude. In a simple linear cavity of length $L$, this translates to longitudinal modes separated by the free spectral range $\Delta\nu \equiv c/2L$. For a ring resonator, the free spectral range is defined by $\Delta\nu \equiv c/L$. The modes wavelengths are determined by the linewidth of the atomic transition in the gain medium.

Laser action occurs when modes with gain exceeding losses amplify in intensity. To minimize losses in solid-state lasers, several factors must be considered: the high reflectivity of the mirrors, appropriate partial reflectivity of the output mirror, reduction of reflection in intra-cavity elements (including the gain medium), the distance between mirrors, the curvature radius of the mirrors, astigmatism compensation, and thermal lensing effects.

In continuous wave (CW) operation, numerous longitudinal modes can coexist within the cavity, each with random relative phases. These modes interfere randomly, resulting in a continuous intensity output characterized by periodicity corresponding to the cavity's round-trip time. In contrast, mode-locking (ML) occurs when multiple longitudinal modes oscillate with well-defined phase relationships, unlike the random phases in CW operation. This phase coherence leads to constructive interference, briefly forming high-peak intensity pulses. The spacing between these pulses, $f_{rep}$, equals the free spectral range. Essentially, mode-locking concentrates electromagnetic energy, which would typically disperse over an extended duration, into exceptionally short pulses oscillating within the cavity.

There are two methods to synchronize the phases of longitudinal modes for mode-locking: active mode coupling, using an oscillating external voltage applied to an acousto-optic or electro-optic modulator, and passive mode coupling, achieved through a saturable absorber (such as a semiconductor saturable absorber mirror, SESAM) or the optical Kerr effect, where a self-focusing material is placed in an aperture, as focused on in this work.

Over time, ML lasers reach a stable state, although limiting factors such as dispersion and gain bandwidth play a role. These factors result in a stable circulating pulse within the resonator. Qualitatively, pulse formation is understood as a balance between pulse shortening due to nonlinear

doi:10.20944/preprints202501.0318.v1

effects, which diminish as the pulse shortens, and the finite gain bandwidth of the active medium, which acts as a pulse-lengthening factor that intensifies as the pulse shortens. Control over factors like astigmatism, dispersion, and thermal lensing is crucial for creating the conditions necessary for generating high-peak intensity pulses, especially in mode-locking, where precise phase relationships are essential. This control ensures that mode-locking maintains its regime over time, making it more effective than continuous wave operation in certain contexts. These factors will be discussed in detail in the following sections.

### 2.1. Astigmatism

In ring-cavity solid-state lasers employing Brewster-angle cut and tilted gain media to minimize surface-reflection loss, an interesting phenomenon occurs. The two transverse components of the Gaussian beam, $x$ (normal to the plane of the cavity) and $y$, propagate through the gain medium at different effective distances. Furthermore, due to the tilt of the cavity's curved mirrors by an angle $2\theta$, they focus parallel rays differently in the two transverse planes. This results in distinct effective focal lengths for the $x$ and $y$ components, inducing astigmatism. Consequently, elliptical Gaussian beams emerge within the folded cavity.

The presence of astigmatism manifests as an elliptical beam, causing power loss during continuous-wave operation and potentially leading to challenges in pulsed mode, such as unstable modes. To rectify astigmatism, adjustments must be made to the angles of reflection for the concave mirrors. The equation governing these adjustments considers two different angles and mirrors of the same radius:

$$\frac{\sin{\theta_1}^2}{\cos\theta_1} + \frac{\sin{\theta_2}^2}{\cos\theta_2} = \frac{2l(n^2-1)}{R}\frac{\sqrt{n^2+1}}{n^4}, \tag{1}$$

where $n$ is the refractive index of the crystal, $l$ is the length of the crystal, and $R$ is the radius of the two concave mirrors [6]. Figure 1 visually illustrates the relationship between $\theta_2$ and $\theta_1$ for a 3 mm Ti:Sapphire crystal, highlighting the influence of mirrors with varying radii. For a cavity with mirrors of the same radius and set at the same reflection angle, the angle can be calculated using the approximation [5]:

$$\sin\theta\tan\theta = \frac{2l(n^2-1)}{R}\frac{\sqrt{n^2+1}}{n^4}. \tag{2}$$

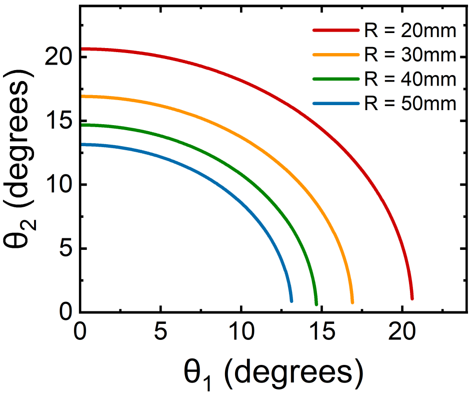

**Figure 1.** Variation of $\theta_2$ as a function of $\theta_1$ for a 3 mm Ti:Sapphire crystal with mirrors of varying radii (R).

### 2.2. Dispersion

Dispersion is a fundamental phenomenon that describes the dependence of a wave's velocity on its frequency or wavelength. When light traverses through a transparent material's lattice structure, it interacts with its particles, experiencing absorption and re-emission, thus delaying its propagation. The Kramers-Kronig relations illustrate the intertwined nature of the absorption interactions and the propagating wave speed, introducing the complex refractive index. In this context, the real part represents the material's refractive index (related to the speed of light propagation), and the imaginary part represents the material's extinction coefficient (related to absorption).

As a pulse propagates through a dispersive material, it can experience spectral phase distortion. In practice, analyzing the spectral phase is often preferred over the temporal phase, as it allows for steady-state analysis. Consequently, the study and characterization of pulses are typically conducted in the spectral domain, facilitating a more straightforward understanding of their behavior. This can be described by expanding the spectral phase $\phi(\omega)$ in a Taylor series around the center frequency $\omega_0$. The zero-order term represents the absolute phase, the first-order term is referred to as the group delay (GD), and the second-order term corresponds to the group-delay dispersion (GDD). Typically, only a few expansion terms suffice to characterize well-behaved pulses, while more complex pulses may require an increased number of terms. The GDD measures the group delay of each different pulse frequency $\omega$, often referred to as chirp. Ultrashort pulses exhibit a broadband spectrum, making this effect significant and introducing phase distortion that increases their duration [31]. This temporal broadening arises from the different dispersion experienced by different frequencies, as the GDD of the material is given by:

$$\mathrm{GDD} \equiv \left.\frac{\mathrm{d}^2\phi(\omega)}{\mathrm{d}\omega^2}\right|_{\omega=\omega_0} = \frac{\lambda^3}{2\pi c}\frac{\mathrm{d}^2}{\mathrm{d}\lambda^2}\mathrm{OP}(\lambda), \tag{3}$$

where $\mathrm{OP}(\lambda)$ is the optical path in the cavity of wavelength $\lambda$. It is important to acknowledge that optical components within a cavity can introduce positive dispersion into the system. In some cases, the pulse broadening by a material can also be measured in GDD per millimeter, termed group velocity dispersion (GVD). The GDD and GVD of a material can be measured using techniques like Frequency-Resolved Optical Gating (FROG) with a known femtosecond pulse.

Maintaining a stable pulse within the optical cavity is crucial, so this dispersive effect must be corrected. To counteract this effect, it becomes necessary to introduce negative dispersion within the cavity. This requirement is typically fulfilled by employing pairs of prisms, diffraction gratings, or specialized dispersion compensation mirrors. These optical elements effectively counterbalance the positive dispersion imposed by other components, thus ensuring the desired pulse properties and overall system performance.

### *2.3. Thermal lensing*

High intensities significantly increase the crystal temperature, leading to a thermal lens effect—a phenomenon where variations in temperature or stress alter the refractive index. This thermal lensing substantially affects the crystal's focal length, which in turn disrupts the alignment of the optical cavity. Furthermore, elevated crystal temperatures can drive the system beyond its optimal operational range, thereby reducing efficiency [8]. In the case of ultrashort pulse lasers, the high intracavity laser intensities impose pronounced thermal effects, even exceeding those caused by the pump, which can critically influence laser performance. Insufficient temperature control may result in diminished performance, failure to achieve the desired operational regime, or even permanent damage to the crystal rod. Understanding the impact of thermal lensing on crystals such as Ti:Sapphire requires comprehensive modeling approaches. Various methods exist to model thermal lensing, including those that account for temperature-dependent thermal conductivity and anisotropies [8,32–34]. Advanced models tailored for high-power amplified systems are also available [35]. Additionally, experimental techniques have been developed to measure and mitigate thermal effects in Brewster-cut Ti:Sapphire crystals, enabling suppression of thermal lensing in high-repetition-rate laser systems and correction of wavefront aberrations for ultrahigh-intensity and metrology applications [36].

To overcome these challenges and ensure stable laser operation, effective thermal management strategies are essential. These strategies often involve implementing advanced cooling systems to regulate the crystal's temperature and maintain it within optimal operating parameters. In ultrashort pulse laser systems, such temperature control measures can effectively mitigate thermal effects, ensuring they remain negligible and preserving the system's performance and integrity.

The cooling mechanisms employed in most solid-state lasers primarily involve liquid cooling systems. These systems effectively manage the thermal energy generated during laser operation. In the case of larger lasers, the excess heat is typically dissipated through two main methods: liquid-to-air heat exchange, where the heat is released into the surrounding air, or liquid-to-liquid heat exchange, where the waste heat is transferred to an external cooling loop [8]. However, for smaller-scale lasers, a different approach is often taken. Here, the thermal energy generated by the pump source and the laser medium is efficiently removed through conduction and subsequently dissipated into the environment via forced air cooling.

In specific laser configurations, the active medium is directly affixed to a heat sink to ensure effective conduction cooling. To achieve optimal thermal conduction, it is imperative to establish intimate thermal contact between the laser medium and the heat sink. This can be accomplished through various means such as mechanical clamping, soldering, or bonding of the laser rod to the heat sink. In instances where mechanical clamping is employed, it's important to note that a temperature gradient may develop across the interface between the laser rod and the clamp. To mitigate this issue, a thin layer of indium foil is often applied between the laser crystal and the copper heat sink. However, for smaller crystals, typically those less than 10mm in size, the use of an indium layer is generally unnecessary and may even pose risks during mounting and alignment procedures, potentially resulting in the inadvertent melting of the indium layer and damage to the crystal.

## 3. Bow-Tie Cavity Design

Analyzing the geometric stability conditions of a resonant cavity holds paramount importance, particularly in the context of laser systems where precise beam control is essential. These conditions are crucial for ensuring the laser operation and desired beam characteristics within the cavity, especially when aiming to model and maintain a small beam spot size. The geometric stability ensures that the laser beam retains its quality and characteristics, allows the modes control, and improves the efficiency of optical components, minimizing losses due to misalignment or other aberrations and maximizing the laser's output power and energy.

An indispensable tool for evaluating and optimizing the geometric stability of a resonant cavity is the Ray Transfer Matrix method. This method provides a comprehensive framework for assessing laser beam propagation through various optical elements within the cavity using ABCD matrices. In this approach, one of the beam waists traverses beneath the crystal, while the other passes between the flat mirrors, as shown in Equation (4). It is particularly valuable for analyzing non-orthogonal optical systems, allowing for detailed examination of beam behavior in both the sagittal and tangential planes.

$$\begin{pmatrix} x_{\text{out}} \\ x'_{\text{out}} \end{pmatrix} = \begin{pmatrix} A & B \\ C & D \end{pmatrix} \begin{pmatrix} x_{\text{in}} \\ x'_{\text{in}} \end{pmatrix} \tag{4}$$

The analysis of the bow-tie design cavity involves a model employing two curved mirrors, functioning as lenses, and two flat mirrors, shown in Figure 2. To scrutinize this ring cavity effectively, it can be conceptualized as a periodic linear lenses sequence [37]. This cavity commences at the location between the planar mirrors, undergoes focusing at the crystal, and eventually returns to the same initial position in a repetitive linear manner, conforming to boundary conditions that maintain its original spot, as illustrated in Figure 3. This condition indicates periodic refocusing of the original beam.

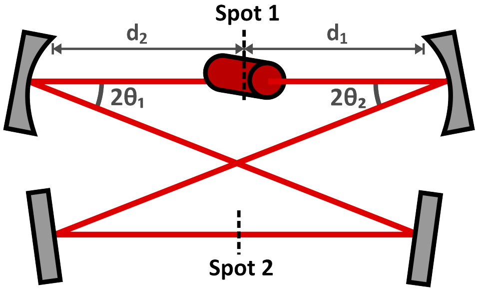

**Figure 2.** Configuration of a typical Kerr-lens mode-locked bow-tie oscillator with two curved mirrors and a Kerr medium. Here, $d_1$ and $d_2$ denotes the distance between each curved mirrors and the crystal center and $\theta_1$ and $\theta_2$ represents the tilt of each curved mirrors.

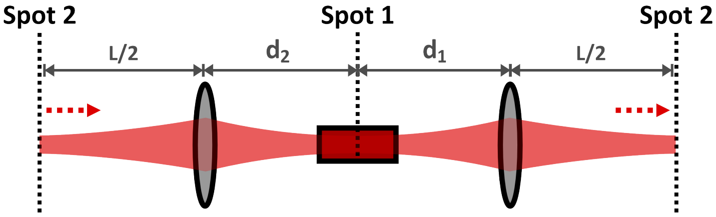

**Figure 3.** The representative model of the bow-tie cavity for the ABCD-matrix calculation. Here, $d_1$ and $d_2$ denotes the distance between each curved mirrors and the crystal center and $L$ represents the overall length in addition to $d_1$ and $d_2$. This image has been adapted from Figure 1 of reference [38].

For the fundamental Gaussian mode (TEM$_{00}$), the approximate solution of the wave equation of the beams leads to an essential relationship involving the complex parameter $q(z)$, which describes the Gaussian variation of beam intensity along the optical axis and the curvature of the phase front, as well as $R(z)$, a real parameter that characterizes the curvature of the wavefront intersecting the axis at position $z$, and $w(z)$, representing the spot size or beam radius:

$$\frac{1}{q_{cw}} = \frac{1}{R} - i\frac{\lambda}{\pi w^2}. \tag{5}$$

In this context, the evolution of a Gaussian beam through an optical system can be assessed using the ABCD law [39]:

$$q_1 = \frac{Aq_2 + B}{Cq_2 + D}. \tag{6}$$

Through the ABCD Law, it is possible to derive the results for the radius of curvature of the wavefront and the beam radius, denoted as $R$ and $w$, respectively, as functions of the system matrix coefficients:

$$R = \frac{2B}{D - A} \quad \text{and} \quad w^2 = \frac{|B|\lambda}{\pi}\sqrt{\frac{1}{1-(A+D)^2/4}}. \tag{7}$$

In the evaluation of a sequence of ABCD matrices, the stability of periodic sequences must satisfy the inequality $-2 < A + D < 2$, as derived from Sylvester's theorem for the beam radius equation [22]. These ABCD matrices represent various optical elements such as free space between components, the curvature of mirrors, and the length of crystals. By evaluating these matrices, the conditions for the existence and stability of the beam radius is determined.

For instance, consider a cavity with two curved mirrors having a radius $R = 30$ mm and a 3 mm-thick Ti:Sapphire crystal. For a 1.0 GHz cavity, the allowable distance between the curved mirrors ranges from 3.13 mm to 3.16 mm. For a 500 MHz cavity, the distance ranges from 3.13 mm to 3.30 mm, and for a 100 MHz cavity, it ranges from 3.13 mm to 3.51 mm, as illustrated in Figure 4.

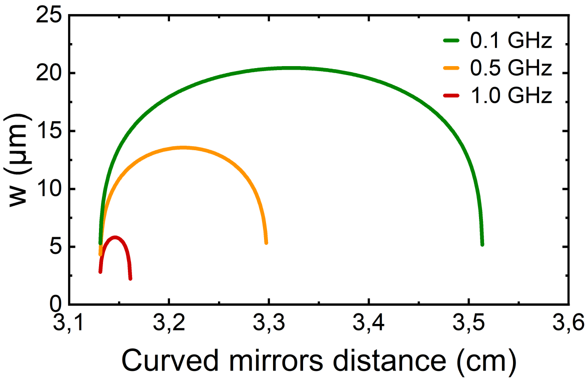

**Figure 4.** Spot size of the laser beam as a function of the distance between the curved mirrors for a 0.1, 0.5 and 1.0 GHz bow-tie cavity, featuring a 3 mm-thick crystal and curved mirrors with a 30 mm radius of curvature

This analysis ensures the beam remains stable within the cavity, meeting the required stability criteria for different parameters. This allows for the evaluation of how various parameters influence the production of a laser beam. For example, it enables the determination of the appropriate radius of curvature for mirrors relative to the cavity length and the optimal positioning of mirrors within the cavity mounting. By assessing these factors, one can optimize the design and alignment of optical components to achieve desired beam properties and stable cavity operation.

### *3.1. Cavity Analysis for Mode-Locked Regime*

To achieve pulsed operation without the need for a saturable absorber, the Kerr effect is harnessed, which is a nonlinear phenomenon capable of altering the refractive index of the crystal in proportion to the incident intensity. This effect is exploited in Kerr lens mode-locking, in which the self-focusing of the crystal induces changes in the beam propagation, dependent on the cavity configuration, for a mode coupling. To optimize the utilization of the crystal's self-focusing effect, it is essential to adjust the crystal's position relative to the curved mirrors' focal points and the distance between the mirrors, maximizing intracavity power and resulting in a reduced beam radius. To quantify the impact of intracavity power ($P$) on the beam radius ($w$), the parameter known as the Kerr lens sensitivity, denoted as $\delta$, is introduced [20] and defined as:

$$\delta = \left[\frac{1}{w}\frac{\mathrm{d}w}{\mathrm{d}P}\right]_{P=0}. \tag{8}$$

An in-depth analysis of the Kerr lens sensitivity concerning the positions of the curved mirrors relative to the crystal within a ring cavity reveals that this parameter approaches negative values near the stability region's boundary. This highlights its remarkable sensitivity to the crystal's placement in relation to the curved mirrors and their separation. The Figure 5 displays a numerically calculated contour plot for $\delta$ at the center of the crystal as a function of the distance between the curved mirrors, $d_1$ and $d_2$ in Figures 2 and 3, and the crystal. Within the stability region, there exists only a small area where the parameter $\delta$ tends towards infinity, close to the inner stability region, where the mirrors are closer to the crystal. For a symmetric cavity with the crystal at the cavity's center, the region where $\delta < 0$ spans approximately 0.3 mm, as illustrated in Figure 6. When a Ti:sapphire laser cavity is adjusted to be within this region, it operates in a stable mode-locked regime with minimal disruptions, eliminating the need for introducing slits or any other element to induce saturable absorption.

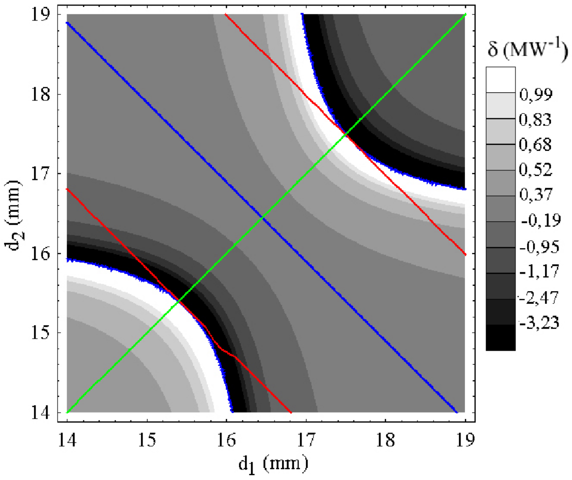

**Figure 5.** Numerically calculated contour plot for Kerr lens sensitivity at the crystal's center as a function of the distance between the curved mirrors and the crystal for a 1GHz ring cavity with a 3 mm-thick crystal and curved mirrors with a radius of curvature of 30 mm. The red curve delineates the stability region, the blue curve represents the point where $\delta$ equals zero, and the green curve corresponds to $d_1 = d_2$.

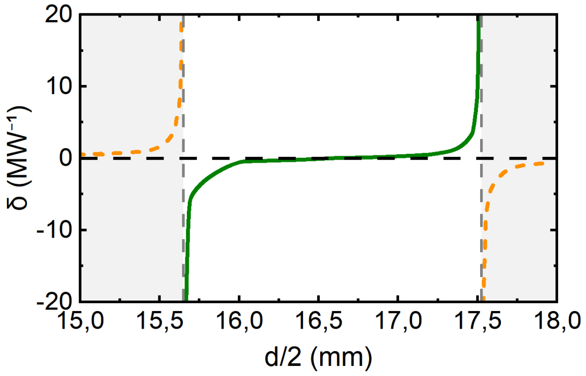

**Figure 6.** Numerically calculated Kerr lens sensitivity at the crystal's center as a function of the distance between the curved mirrors and the crystal for a symmetric 1 GHz ring cavity with $d_1 = d_2 = d/2$, featuring a 3 mm-thick crystal and curved mirrors with a 30 mm radius of curvature. The gray regions indicate unstable regions, while the non-gray region indicate stable region.

## 4. Experimental Setup

The optical components used in the laser cavity are a Ti:Sapphire crystal as a gain medium, a focus lens (L1) with a focal length $f$ = 50 mm for focusing the beam on the crystal, two concave dispersive mirrors M1 and M2 of radius $R$ = 30 mm, a plane dispersive mirror (P1) and an flat output mirror (OC), with 98% reflection for 660-920 nm, arranged in a ring shape shown in the Figure 7. The 3 mm thick crystal, shown in Figure 8, used in this laser system has the linear index of refraction $n_0(\lambda)$ = 1.772 for 532 nm and $n_0(\lambda) = 1.760$ for 800 nm and exhibits an absorption in the blue-green spectrum with a maximum at 500 nm and an emission in the near-infrared range with a maximum at 800 nm, with the spectrum measured in Figure 9. The crystal is cut at the Brewster angle forming an angle of 60.4° between the pumping incidence surface and the side. The pump used is a frequency-doubled Nd:YAG laser with emission at 532 nm. For the spherical mirrors and crystal used in the system, the astigmatism compensation angle is approximately $\theta$ = 24°.

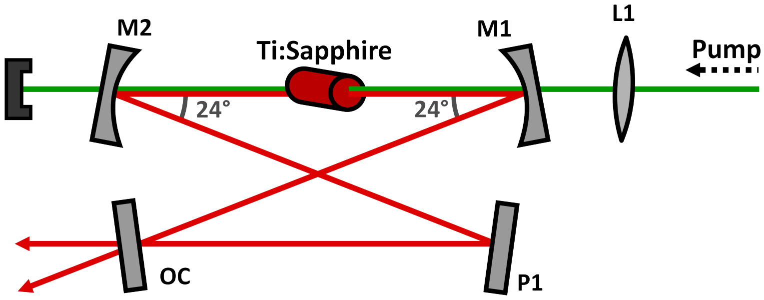

**Figure 7.** Diagram of the bow-tie laser cavity. The Ti:Sapphire crystal is positioned between two concave dispersive mirrors with a 30 mm radius of curvature. There are two flat mirrors, one of which is the output coupler with 98% reflection for 660-920 nm.

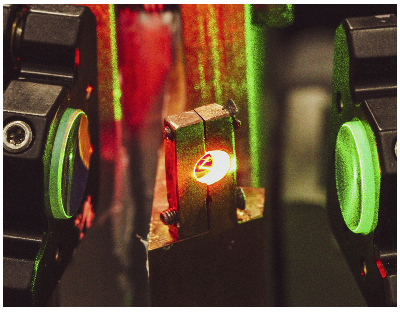

**Figure 8.** Photograph of the Ti:Sapphire crystal between two curved dispersion compensation mirrors (M2 on the left and M1 on the right).

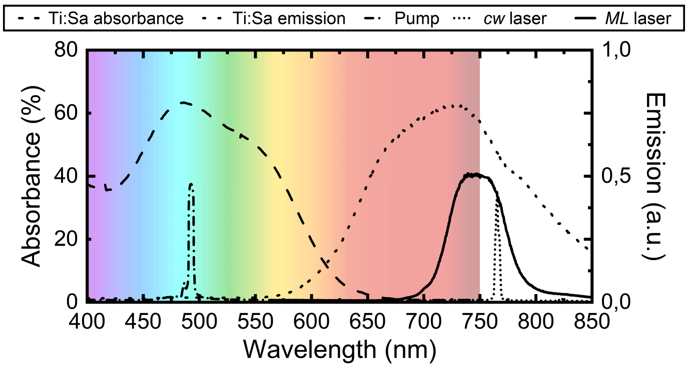

**Figure 9.** Spectrum of Ti:Sapphire crystal absorbance (dashed) and emission (dotted), pump laser Nd:YAG (dot-dashed), *CW* peak of Ti:Sapphire laser (short dotted), and mode-locked laser emission (solid).

The crystal is precisely cut at the Brewster angle to optimize the transmission of the linearly polarized pump beam. This configuration ensures that the pump beam, prior to entering the cavity, traverses two mirrors to align its path with the optical table, followed by its passage through polarizers. The goal is to enhance transmission through the crystal while minimizing unwanted reflections. For meticulous adjustments, a powermeter is employed to measure the power of the reflected pump beam, enabling precise calibration of the polarizer to achieve the lowest power output.

In order to mitigate the positive GDD exhibited by the crystal, which averages at +180 $fs^2$, Dispersion-Compensating Mirrors (DCMs) were employed, which are multilayer structures designed to provide a larger delay for longer wavelengths, enabling the generation of laser pulses with minimal distortion. The DCMs are characterized by a GDD of -70 (±30) $fs^2$, marked by substantial oscillations across various wavelengths. White-light interferometry (depicted in Figure 10) validates the presence of significant GDD variations. Using mirror pairs with intentionally designed opposing oscillations, the resulting combined GDD exhibits a smooth spectral profile, effectively rectifying any oscillatory behavior [3,11]. The results demonstrate the absence of significant dispersion issues or tuning difficulties in achieving the modelocked regime. DCMs effectively provide compensation [24,25] without requiring an increase in the number of optical elements or the size of the cavity.

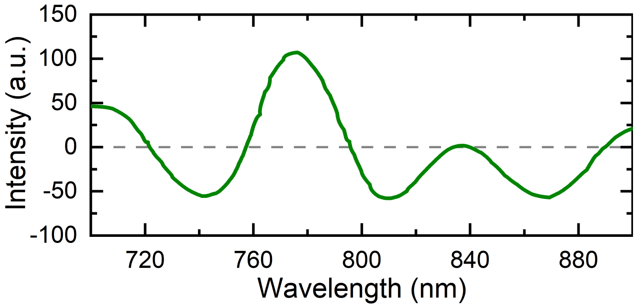

**Figure 10.** Net group delay dispersion (GDD) characterization of the entire optical cavity, featuring three dispersion-compensating mirrors, the crystal, and the output coupler, determined through white-light interferometry. This image is adapted from Figure 1 of reference [24].

To mitigate the impact of thermal effects, cooling systems can be affixed to support the crystal. The crystal was securely clamped to a copper plate, as depicted in Figure 8. A conduction cooling strategy was implemented by employing a Peltier thermoelectric cooling module coupled with an air-cooled heatsink. This arrangement effectively ensured a thermally stable operating temperature range for the crystal, maintaining temperatures within the 18°C to 28°C range while minimizing temperature fluctuations to less than 2°C [40]. This temperature stability, in turn, resulted in a consistent laser efficiency over time, as depicted in Figure 11.

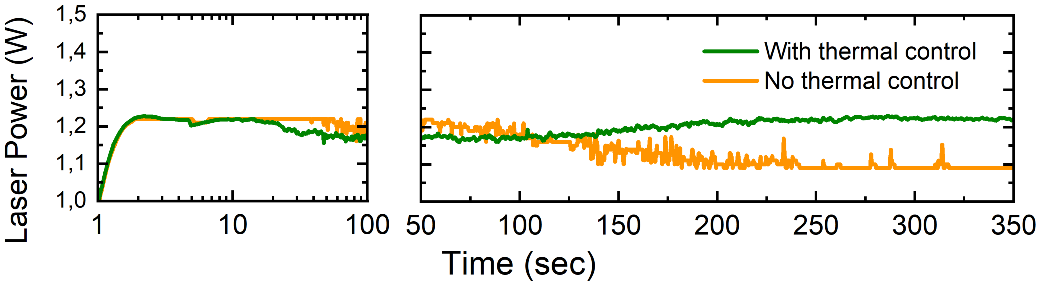

**Figure 11.** Temporal evolution of *CW* laser power (a) with Peltier cooling system (green curve) and (b) without cooling (orange curve). The initial power drop in both scenarios is attributed to crystal heating, followed by power stabilization. The Peltier cooling system demonstrates more efficient power stabilization by maintaining lower crystal temperatures when the system reaches thermal equilibrium.

As an option, a PZT ceramic can induce the modelock regime by attaching it to the P1 mirror. Control electronics can be developed that allow the repetition rate to be stabilized in relation to an internal generator, with a fine tuning of up to 30 kHz with input for an external oscillator. This setup also allows wavelength tuning in the 770 nm to 810 nm range [24,41].

## 5. Laser Fine-Tuning for Optimal Performance

To ensure optimal performance, the optical components were evaluated for cleanliness and surface grooves prior to assembly, following the manufacturer's recommended cleaning procedures when available. Maintenance and cleaning of the laser system are of paramount importance, especially during Mode-locking operation. In mode-locking operation, the laser system becomes significantly more sensitive to contaminants and dirt compared to CW operation. Therefore, meticulous attention is required when aligning the components and ensuring that the cavity remains isolated from contamination and dirt. Utilizing indium in small crystals, as discussed earlier, may result in crystal damage due to overheating, as illustrated in Figure 12. For crystal defects or grooves, polishing was performed using Diamond Lapping Film (0.1-10 $\mu$m). For plane mirrors that exhibit grooves, the scratched regions are avoided for laser incidence. No scratched spherical mirrors and scratched lenses were used to ensure accurate reflection and propagation without scattering. Component cleaning procedures were performed by blowing the surface with a pure duster or using appropriate lens cleaning wipes with solvents such as acetone, methanol or isopropanol.

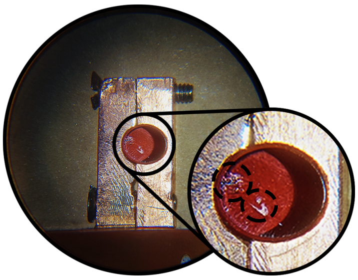

**Figure 12.** Enlarged photograph of the Ti:Sapphire crystal reveals grooves and defects, indicated by dashed circles, which have arisen due to the overheating of an Indium layer.

All optical components must be at the same height as the pumping beam. Slits or rulers can serve as references for this purpose. The pump and intracavity laser need to be centered on spherical mirrors and lenses to avoid aberrations, whereas flat mirrors do not require precise centering. The pumping beam height was standardized at h = 120 mm.

The initial alignment is essential to ensure that the laser beam is at the same height as the optical table, without any bending. This alignment is crucial for the correct and optimal executions of subsequent steps. To achieve coplanarity, it is recommended to utilize a pair of circular precision pinholes placed at the designated height along the beam path. Each optical component should be aligned by positioning it in such a way that the beam passes through the center of the two pinholes. By maintaining consistent heights for the pump beam, intracavity beam, and output beams throughout the entire cavity, there will be no need for vertical realignment, except for minor adjustments that may be required.

During the assembly and alignment process, distances between the mirrors and the crystal were measured using a digital caliper with the pump turned off. Care was taken to handle only the optical component supports to prevent damage. While this method provides reasonable precision, it may not be feasible in all setups. In such cases, alternative methods, such as observing luminescence reflections from the crystal on mirrors M1 and M2, can be employed. Precision at this stage is not critical, as further adjustments will be required to optimize laser performance, as detailed below.

### *5.1. Achieving and Optimizing the Laser Action*

The mirrors must be aligned in such a way that they reflect the laser beam correctly, as illustrated in the laser schematic Figure 7. Moreover, it is crucial to ensure that the round-trip reflections of the laser beam fall on the same point, which can be achieved by centering the optical components on the height of the pump. This alignment process requires meticulous adjustment of the mirrors to minimize losses and optimize system efficiency.

Once the reflections are centered correctly, the laser emission threshold can be achieved through the angle adjustments made in the mirror mounts. The laser can be observed to emit different transverse electromagnetic (TEM) modes, but the desired outcome is the $\text{TEM}_{00}$ mode, which exhibits a Gaussian circular pattern and requires careful tuning of the mirrors [5]. The observation of the $\text{TEM}_{00}$ mode is indicative of good alignment.

After achieving laser action, optimizing the laser involves finding the ideal reflection distances and angles. This involves scanning the positions of the crystal and M2 mirror and making angular corrections through the mirror mounts. The incidence of the intracavity beam on the mirrors indicates the alignment quality: misaligned beams are off-center on the spherical mirrors, as shown in Figure 13a, whereas aligned beams are centered on the curved mirrors, as depicted in Figure 13b. This can be easily corrected with flat mirror correction, in order to bring the beam closer to the center of the spherical mirrors.

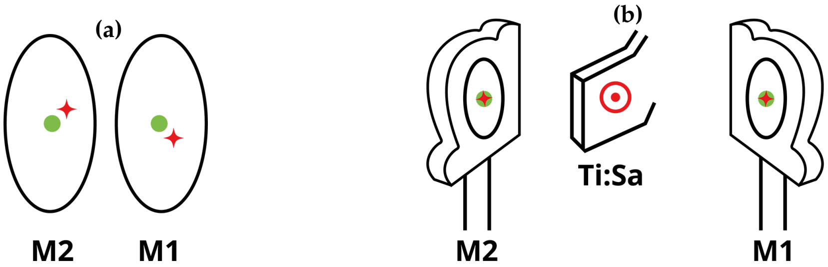

**Figure 13.** Example of (a) misaligned beam with vertical and horizontal variation and (b) aligned beam centered on M1 and M2 the spherical mirrors.

Alignment progress can be monitored using a powermeter to observe increases (indicating good alignment) or decreases (indicating poor alignment) in output beam power. During optimization, laser emission is more prominent, and other reflections around the spot tend to be weaker, as illustrated in Figure 14. However the behavior of the output beam can vary depending on the emission wavelength, if the laser emission varies to a wavelength closer to the NIR, it may not be perceptible to the naked eye. Therefore, the powermeter measurement remains the most reliable indicator of alignment progress.

**Figure 14.** Output laser beam patterns observed on a bulkhead during laser emission threshold (left) to optimized laser emission (right).

Astigmatism can experimentally deviate from the value predicted by the equation due to changes in temperature and other parameters. This can be adjusted by analyzing if the output beam profile is circular and power measurement is rising. To optimize astigmatism compensation, it is necessary to scan around the estimated reflection angle and explore variations to achieve better results. In our case, angles slightly smaller than the estimated 24° provided optimal results.

After determining the optimal power for various angle and position tests, it is crucial to record the positions and distances of the optical components for future reference, if necessary.

### *5.2. Achieving the Modelock Regime*

In order to achieve the modelock regime, a scanning procedure was carried out to optimize the focus from the continuous wave regime to the pulsed regime. This involved adjusting the positions of the M2 mirror and the crystal, bringing them closer to the M1 mirror, with the intention to decrease the confocal parameter of the cavity. During the scanning process, small variations in power density were induced through mechanical vibrations in the P1 mirror or in the OC mirror, and the behavior of the spectrum of the output beams was observed.

The scanning process is cyclical and begins with the laser optimized with the best power. Initially, bringing the M2 mirror slightly closer to the crystal was sufficient to observe instabilities between the regimes during the process, as represented in Figure 15. These instabilities may appear in more than one position along the scan, but they will only be present if the cavity is properly aligned to achieve the pulsed regime. Therefore, after approaching mirror M2 and identifying the instability region closest to the crystal, the crystal was moved closer to mirror M1 so that the broad band in the spectrum is still observed. The intention of the alignment at this moment is to bring the mirror M2 and the crystal closer to the mirror M1 in the region where the instability in the spectrum is observed, bringing the cavity closer and closer to the stability limit. Once the approximation limit is reached, it is necessary to make corrections in the plane mirrors and in the pumping focus lens (without changing the position of the spherical mirrors and the crystal) in order to make the broadband more stable and without CW peaks. By increasing the distance from the pumping lens to the crystal, the focus of the lens moves closer to the M1 mirror, which allows you to continue to zoom in on the crystal and the M2 mirror as well. The scanning process is then continued with the M2 mirror, bringing it closer to the M1 mirror, repeating the previous steps. Please note that the process must be carried out carefully and slowly.

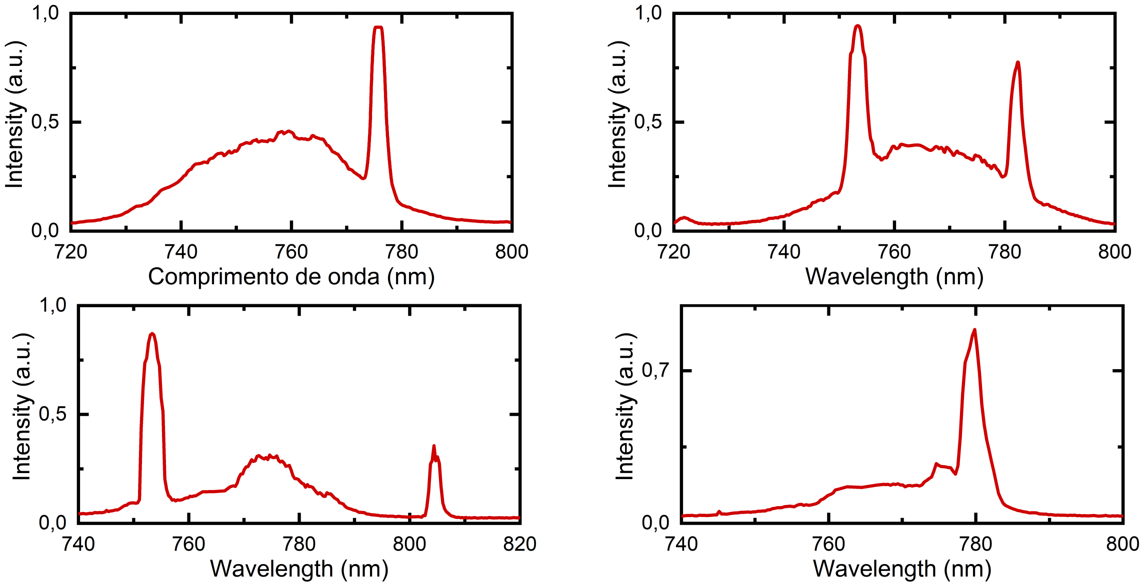

**Figure 15.** Spectrum of the laser output beam in the intersection between the continuous-wave, characterized by peaks, and modelock regimes, characterized by a regular broadband.

It is important to note that the laser output beam power decreases significantly during the process. When the laser achieves stable broadband emission without any continuous wave laser peaks and only one output laser beam is present, it indicates the attainment of the mode-locked regime. In regions of instability within the cavity's broadband spectrum, the laser beam appears as a "hazy beam", which differs from the standard beam observed in continuous wave lasers.

## 6. Experimental Results

After aligning the mirrors to achieve laser action, the alignment was optimized in continuous wave operation. In the optimized configuration, the lasing threshold was reached at a pump beam power of 0.4 W, and the output-to-pump power ratio was approximately 25% for pump powers above 2 W, as shown in Figure 16. The output-to-pump ratio for CW operation indicated that the CW alignment was optimized to facilitate mode-locking alignment. With the output-to-pump power ratio indicating good performance in CW mode, a specific pump power was set for alignment in the mode-locking regime. It is important to note that the pump power must remain fixed because any variation would necessitate realigning the system to achieve mode-locking.

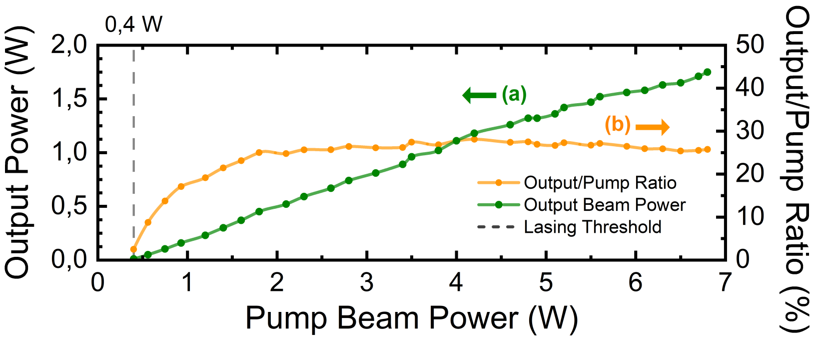

**Figure 16.** Measurements of lasing threshold at a pumping power of 0.4W, including the average power of the output beam and its ratio to the average power of the pumping beam, both represented in green and orange, respectively, for laser emission in the continuous-wave regime.

By further optimizing the alignment for mode-locked laser action, it was possible to achieve the mode-locking regime at a pump power of 7.4 W, generating output pulses with an average power of 0.94 W. The output-to-pump ratio achieved was 12.7%, the same as reported in [41] and greater than the approximately 8% reported in [24,42,43] for the Ti:Sapphire rings cavities. The spectrum measured with a spectrometer, as shown in Figure 17, exhibited a Gaussian shape with $R^2 = 0.994$, centered at 756 nm with a full width at half maximum (FWHM) of 42 nm, indicating the potential for Gaussian transform-limited pulses of 20 fs. The intensity autocorrelation trace, measured using the Frequency-Resolved Optical Gating (FROG) technique and shown in Figure 18, indicated a pulse duration of 61 fs. These results show a time-bandwidth product of 1.34, suggesting a pulse with low dispersion that can be further improved by using better DCMs or by integrating pulse compression systems. The radio-frequency (RF) spectrum, depicted in Figure 19, indicated a pulse repetition rate of 1.03 GHz.

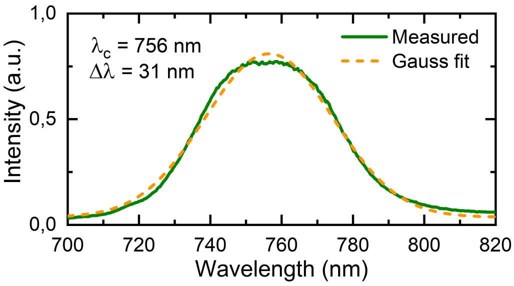

**Figure 17.** Spectrum of the laser output beam in the modelock regime centered at 756 nm and with a FWHM of approximately 42nm.

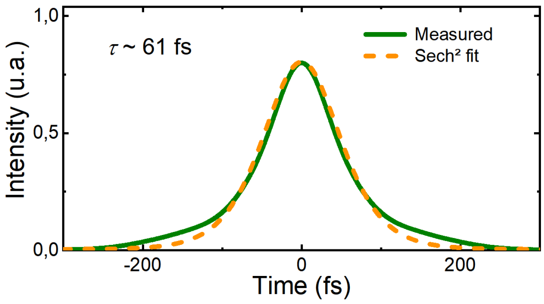

**Figure 18.** Intensity autocorrelation trace of the pulse and its sech² fit

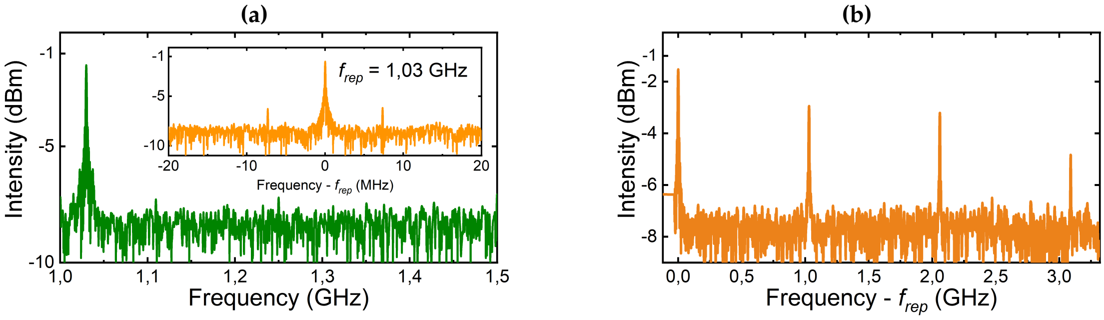

**Figure 19.** (a) Radio-frequency (RF) spectrum of the laser fundamental repetition rate $f_{rep}$ = 1,03 GHz. Inset: RF spectrum centered at $f_{rep}$ with 40Hz spam. (b) RF spectrum of the higher repetition rate harmonics measured.

## 7. Discussion and Conclusion

The bow-tie configuration of this compact cavity, combined with the use of dispersion-compensating mirrors, is a critical factor in achieving pulse repetition rates on the order of GHz. This design reduces the size of the cavity while maintaining excellent beam quality and stability. The choice of pump laser significantly influences oscillator performance, cost, and size. Frequency-doubled diode-pumped solid-state lasers (DPSSLs) remain the most common pump sources for Ti:Sapphire oscillators due to their high output power, beam quality, and durability. However, their complexity, large dimensions, and water cooling requirements contribute to increased size and cost. Recent advancements have demonstrated the potential of alternative pump sources, such as frequency-doubled tapered diode lasers [44], optically pumped semiconductor (OPS) lasers [45], and semiconductor laser diodes (LDs) [46–48]. These alternatives offer advantages such as compactness, efficiency, and lower costs. For instance, green-LD pumps, with emission closer to the Ti:Sapphire absorption peak, have shown promising results in delivering higher efficiency compared to blue-LD pumps. Dual-color LD systems aim to mitigate pump-induced losses from blue-LD pumps, but challenges remain, including limited output power and complex kinetic processes that necessitate further optimization [48,49]. While these pump alternatives excel in compactness, affordability, and efficiency, their limited output power restricts their suitability to applications with moderate energy needs or exploratory research. For high-energy-demanding applications or precision experiments requiring high pulse energies, DPSSLs remain the safest choice. Ultimately, the pump source must align with the specific goals and requirements of the Ti:Sapphire oscillator. However, Yb-doped diode-pumped solid-state lasers (Yb-DPSSLs), which use Yb-doped crystals instead of Ti:Sapphire, can achieve higher output powers, expanding the potential for applications requiring more energy [23]. Meanwhile, DCMs play a critical role in achieving ultrashort pulse durations by counteracting dispersion effects without requiring additional optical elements like prisms. The inclusion of Peltier-based temperature control enhances system stability and ensures long-term crystal preservation, offering a low-cost and compact solution for thermal management [40]. Fine-tuning the alignment results in a mode-locked laser generating 61 fs pulses with an average power of 0.94 W and a 1 GHz repetition rate, yielding an approximate pulse energy of 1 nJ and a peak power of 15 kW. By leveraging these design elements, the compact cavity offers a versatile and reliable platform for ultrafast laser applications, with potential for further improvements and customization. Enhancements such as improved DCM-crystal tuning and integrated pulse compression systems can achieve sub-10 fs pulses [41]. Additionally, variations such as photonic-circuit-integrated lasers offer advantages of high portability and minimal power consumption [50]. By addressing experimental and practical aspects often not fully detailed in the literature, the alignment and stabilization procedures detailed in this work, combined with the provided tools, discussions, and guidelines, serve as a resource for researchers and engineers seeking to develop high-performance compact cavities in a more time-efficient manner.

**Author Contributions:** Conceptualization, Vinícius Pinto; Data curation, Vinícius Pinto; Formal analysis, Vinícius Pinto; Funding acquisition, Fátima Yasuoka and Jarbas Neto; Investigation, Vinícius Pinto; Methodology, Vinícius Pinto and Giovana Nogueira; Project administration, Fátima Yasuoka and Jarbas Neto; Resources, Fátima Yasuoka and Jarbas Neto; Software, Vinícius Pinto and Giovana Nogueira; Supervision, Giovana Nogueira, Fátima Yasuoka and Jarbas Neto; Validation, Vinícius Pinto; Visualization, Vinícius Pinto; Writing – original draft, Vinícius Pinto; Writing – review & editing, Vinícius Pinto, Giovana Nogueira, Fátima Yasuoka and Jarbas Neto. All authors will be updated at each stage of manuscript processing, including submission, revision, and revision reminder, via emails from our system or the assigned Assistant Editor.

**Funding:** This research was funded by State of Sao Paulo Research Foundation (FAPESP) grant numbers #2015/15990-1, #2021/08202-8, and #2013/07276-1 (CEPOF-CEPID Program), and Coordination of Higher Education Personnel Improvement (CAPES) grant number 88887.894931/2023-00.

**Institutional Review Board Statement:** Not applicable.

**Informed Consent Statement:** Not applicable.

**Data Availability Statement:** Data underlying the results presented in this paper are not publicly available at this time but may be obtained from the authors upon request.

**Acknowledgments:** To the State of Sao Paulo Research Foundation (FAPESP) through research funding grants #2015/15990-1, #2021/08202-8, and #2013/07276-1 (CEPOF-CEPID Program), and the Coordination of Higher Education Personnel Improvement (CAPES) through research funding grant 88887.894931/2023-00. Without FAPESP and CAPES, this research would not have been possible, and therefore, we acknowledge the entire Brazilian society for paying their taxes to support science.

**Conflicts of Interest:** The authors declare no conflicts of interest. The funders had no role in the design of the study; in the collection, analyses, or interpretation of data; in the writing of the manuscript; or in the decision to publish the results.

## References

1. Moulton, P.F. Spectroscopic and laser characteristics of Ti:$Al_2O_3$. *J. Opt. Soc. Am. B* **1986**, *3*, 125–133. https://doi.org/doi:10.1364/JOSAB.3.000125.
2. Xu, L.; Spielmann, C.; Krausz, F.; Szipöcs, R. Ultrabroadband ring oscillator for sub-10-fs pulse generation. *Opt. Lett.* **1996**, *21*, 1259–1261. https://doi.org/10.1364/OL.21.001259.
3. Chen, L.; Yang, W.; Wang, X.; Zhang, Z. Integrative optimization of chirped mirrors for intracavity dispersion compensation. *Optics Communications* **2009**, *282*, 617–620. https://doi.org/https://doi.org/10.1016/j.optcom.2008.10.056.
4. Kalashnikov, V.; Podivilov, E.; Chernykh, A.; Apolonski, A. Chirped-pulse oscillators: theory and experiment. *Applied Physics B* **2006**, *83*, 503–510. https://doi.org/10.1007/s00340-006-2214-1.
5. Shank, H.K.E.I.A.D.C. Astigmatically compensated cavities for CW dye lasers. *IEEE J. QE* **1972**, *8*, 373–379. https://doi.org/10.1109/JQE.1972.1076964.
6. Lin, K.H.; Lai, Y.; Hsieh, W.F. Simple analytical method of cavity design for astigmatism-compensated Kerr-lens mode-locked ring lasers and its applications. *J. Opt. Soc. Am. B* **1995**, *12*, 468–475. https://doi.org/10.1364/JOSAB.12.000468.
7. Abitan, H.; Skettrup, T. Laser resonators with several mirrors and lenses with the bow-tie laser resonator with compensation for astigmatism and thermal lens effects as an example. *Journal of Optics A: Pure and Applied Optics* **2004**, *7*, 7. https://doi.org/10.1088/1464-4258/7/1/002.
8. Koechner, W. *Solid-State Laser Engineering*, 5 ed.; Vol. 1, *Springer Series in Optical Sciences*, Springer: New York, 2006.
9. Brabec, T.; Spielmann, C.; Curley, P.F.; Krausz, F. Kerr lens mode locking. *Opt. Lett.* **1992**, *17*, 1292–1294. https://doi.org/10.1364/OL.17.001292.
10. Masada, G. Miniaturization of an Optical Parametric Oscillator with a Bow-Tie Configuration for Broadening a Spectrum of Squeezed Light. In Proceedings of the Tamagawa University Quantum ICT Research Institute Bulletin, 2012, Vol. 12, pp. 11–14.
11. Yefet, S.; Pe’er, A. A Review of Cavity Design for Kerr Lens Mode-Locked Solid-State Lasers. *Applied Sciences* **2013**, *3*, 694–724. https://doi.org/10.3390/app3040694.

12. Consolino, L.; Campa, A.; Mazzotti, D.; Vitiello, M.S.; De Natale, P.; Bartalini, S. Bow-Tie Cavity for Terahertz Radiation. *Photonics* **2019**, *6*. https://doi.org/10.3390/photonics6010001.
13. Kimura, S.; Tani, S.; Kobayashi, Y. Kerr-lens mode locking above a 20 GHz repetition rate. *Optica* **2019**, *6*, 532–533. https://doi.org/10.1364/OPTICA.6.000532.
14. Ostapenko, H.; Mitchell, T.; Castro-Marin, P.; Reid, D.T. Three-element, self-starting Kerr-lens-modelocked 1-GHz Ti:sapphire oscillator pumped by a single laser diode. *Opt. Express* **2022**, *30*, 39624–39630. https://doi.org/10.1364/OE.472533.
15. Jirauschek, C.; Kärtner, F.X.; Morgner, U. Spatiotemporal Gaussian pulse dynamics in Kerr-lens mode-locked lasers. *J. Opt. Soc. Am. B* **2003**, *20*, 1356–1368. https://doi.org/10.1364/JOSAB.20.001356.
16. Agnesi, A. Kerr-lens modelocking of solid-state lasers and unidirectional ring cavities. *IEEE Journal of Quantum Electronics* **1994**, *30*, 1115–1121. https://doi.org/10.1109/3.291380.
17. Brabec, T.; Curley, P.F.; Spielmann, C.; Wintner, E.; Schmidt, A.J. Hard-aperture Kerr-lens mode locking. *J. Opt. Soc. Am. B* **1993**, *10*, 1029–1034. https://doi.org/10.1364/JOSAB.10.001029.
18. Georgiev, D.; Herrmann, J.; Stamm, U. Cavity design for optimum nonlinear absorption in Kerr-lens mode-locked solid-state lasers. *Optics Communications* **1992**, *92*, 368–375. https://doi.org/https://doi.org/10.1016/0030-4018(92)90647-A.
19. Magni, V. Perturbation theory of nonlinear resonators with an application to Kerr-lens mode locking. *J. Opt. Soc. Am. B* **1996**, *13*, 2498–2507. https://doi.org/10.1364/JOSAB.13.002498.
20. Magni, V.; Cerullo, G.; De Silvestri, S. Closed form gaussian beam analysis of resonators containing a Kerr medium for femtosecond lasers. *Optics Communications* **1993**, *101*, 365–370. https://doi.org/https://doi.org/10.1016/0030-4018(93)90731-J.
21. Cerullo, G.; Silvestri, S.D.; Magni, V.; Pallaro, L. Resonators for Kerr-lens mode-locked femtosecond Ti:sapphire lasers. *Opt. Lett.* **1994**, *19*, 807–809. https://doi.org/10.1364/OL.19.000807.
22. Hodgson, N.; Weber, H. *Laser Resonators and Beam Propagation: Fundamentals, Advanced Concepts and Applications*; Springer New York, 2005. https://doi.org/10.1007/b106789.
23. Zheng, L.; Tian, W.; Liu, H.; Wang, G.; Bai, C.; Xu, R.; Zhang, D.; Han, H.; Zhu, J.; Wei, Z. 2-GHz watt-level Kerr-lens mode-locked Yb:KGW laser. *Opt. Express* **2021**, *29*, 12950–12957. https://doi.org/10.1364/OE.424139.
24. Nogueira, G.T.; Cruz, F.C. Efficient 1 GHz Ti:sapphire laser with improved broadband continuum in the infrared. *Opt. Lett.* **2006**, *31*, 2069–2071. https://doi.org/10.1364/OL.31.002069.
25. Fortier, T.M.; Bartels, A.; Diddams, S.A. Octave-spanning Ti:sapphire laser with a repetition rate >1 GHz for optical frequency measurements and comparisons. *Opt. Lett.* **2006**, *31*, 1011–1013. https://doi.org/10.1364/OL.31.001011.
26. Falconieri, M.; Salvetti, G..; Salvetti, G..; Salvetti, G. Simultaneous measurement of pure-optical and thermo-optical nonlinearities induced by high-repetition-rate, femtosecond laser pulses: application to CS2. *Applied Physics B* **1999**, *69*, 133–136. https://doi.org/10.1007/s003400050785.
27. Tan, B.; Dalili, A.; Venkatakrishnan, K.; Venkatakrishnan, K. High repetition rate femtosecond laser nano-machining of thin films. *Applied Physics A* **2009**, *95*, 537–545. https://doi.org/10.1007/s00339-008-4938-8.
28. Ehlers, A.; Riemann, I.; Martin, S.; Le Harzic, R.; Bartels, A.; Janke, C.; König, K. High (1GHz) repetition rate compact femtosecond laser: a powerful multiphoton tool for nanomedicine and nanobiotechnology. *Journal of Applied Physics* **2007**, *102*, 014701. https://doi.org/10.1063/1.2745367.
29. Latz, C.; Asshauer, T.; Rathjen, C.; Mirshahi, A. Femtosecond-Laser Assisted Surgery of the Eye: Overview and Impact of the Low-Energy Concept. *Micromachines* **2021**, *12*. https://doi.org/10.3390/mi12020122.
30. Chu, S.W.; Liu, T.M.; Sun, C.K.; Lin, C.Y.; Tsai, H.J. Real-time second-harmonic-generation microscopy based on a 2-GHz repetition rate Ti:sapphire laser. *Opt. Express* **2003**, *11*, 933–938. https://doi.org/10.1364/OE.11.000933.
31. Trebino, R. *Frequency-Resolved Optical Gating: The Measurement of Ultrashort Laser Pulses*; Springer US, 2000. https://doi.org/10.1007/978-1-4615-1181-6.
32. Innocenzi, M.E.; Yura, H.T.; Fincher, C.L.; Fields, R.A. Thermal modeling of continuous-wave end-pumped solid-state lasers. *Applied Physics Letters* **1990**, *56*, 1831–1833. https://doi.org/10.1063/1.103083.
33. Frauchiger, J.; Albers, P.; Weber, H. Modeling of thermal lensing and higher order ring mode oscillation in end-pumped C-W Nd:YAG lasers. *IEEE Journal of Quantum Electronics* **1992**, *28*, 1046–1056. https://doi.org/10.1109/3.135227.
34. Wagner, G.; Shiler, M.; Wulfmeyer, V. Simulations of thermal lensing of a Ti:Sapphire crystal end-pumped with high average power. *Optics Express* **2005**, *13*, 8045. https://doi.org/10.1364/opex.13.008045.

35. Cho, S.; Jeong, J.; Hwang, S.; Yu, T.J. Thermal lens effect model of Ti:sapphire for use in high-power laser amplifiers. *Applied Physics Express* **2018**, *11*, 092701. https://doi.org/10.7567/apex.11.092701.
36. Hussain, M.; Imran, T.; Börzsönyi, A. Thermal lensing measurements of Ti: sapphire crystal by an optical wavefront sensor. *Microwave and Optical Technology Letters* **2019**, *61*, 2901–2909. https://doi.org/10.1002/mop.31962.
37. Kogelnik, H.; Li, T. Laser Beams and Resonators. *Appl. Opt.* **1966**, *5*, 1550–1567. https://doi.org/10.1364/AO.5.001550.
38. Xia, P.; Kuwata-Gonokami, M.; Yoshioka, K. Geometrical analysis of Kerr-lens mode-locking for high-peak-power ultrafast oscillators. *Japanese Journal of Applied Physics* **2020**, *59*, 062002. https://doi.org/10.35848/1347-4065/ab9278.
39. Kogelnik, H. Imaging of optical modes — resonators with internal lenses. *Bell System Technical Journal* **1965**, *44*, 455–494.
40. Montalvão, F.F.; de Almeida, I.C.; Pinto, V.P.; de Oliveira, B.P.; Yasuoka, F.M.M.; de Castro Neto, J.C. Peltier-Based Temperature Regulation: A Method for Performance Optimization in Solid-State Lasers. *MethodsX* **2024**, p. 102873. https://doi.org/https://doi.org/10.1016/j.mex.2024.102873.
41. Nogueira, G.T.; Xu, B.; Coello, Y.; Dantus, M.; Cruz, F.C. Broadband 2.12 GHz Ti:sapphire laser compressed to 5.9 femtoseconds using MIIPS. *Opt. Express* **2008**, *16*, 10033–10038. https://doi.org/10.1364/OE.16.010033.
42. Bartels, A.; Dekorsy, T.; Kurz, H. Femtosecond Ti:sapphire ring laser with a 2-GHz repetition rate and its application in time-resolved spectroscopy. *Opt. Lett.* **1999**, *24*, 996–998. https://doi.org/10.1364/OL.24.000996.
43. Chen, L.J.; Benedick, A.J.; Birge, J.R.; Sander, M.Y.; Kärtner, F.X. Octave-spanning, dual-output 2.166 GHz Ti:sapphire laser. *Opt. Express* **2008**, *16*, 20699–20705. https://doi.org/10.1364/OE.16.020699.
44. Le, T.; Müller, A.; Sumpf, B.; Jensen, O.B.; Hansen, A.K.; Andersen, P.E. New class of compact diode pumped sub 10-fs lasers for biomedical applications. In Proceedings of the Frontiers in Ultrafast Optics: Biomedical, Scientific, and Industrial Applications XVI; Heisterkamp, A.; Herman, P.R.; Meunier, M.; Nolte, S., Eds. International Society for Optics and Photonics, SPIE, 2016, Vol. 9740, p. 97400D. https://doi.org/10.1117/12.2208589.
45. Resan, B.; Coadou, E.; Petersen, S.; Thomas, A.; Walther, P.; Viselga, R.; Heritier, J.M.; Chilla, J.; Tulloch, W.; Fry, A. Ultrashort pulse Ti:sapphire oscillators pumped by optically pumped semiconductor (OPS) pump lasers. In Proceedings of the Solid State Lasers XVII: Technology and Devices; Clarkson, W.A.; Hodgson, N.; Shori, R.K., Eds. International Society for Optics and Photonics, SPIE, 2008, Vol. 6871, p. 687116. https://doi.org/10.1117/12.767364.
46. Muti, A.; Kocabas, A.; Sennaroglu, A. 5-nJ Femtosecond Ti3+:sapphire laser pumped with a single 1 W green diode. *Laser Physics Letters* **2018**, *15*, 055302. https://doi.org/10.1088/1612-202X/aaaea7.
47. Liu, H.; Wang, G.; Jiang, J.; Tian, W.; Zhang, D.; Han, H.; Fang, S.; Zhu, J.; Wei, Z. Sub-10-fs pulse generation from a blue laser-diode-pumped Ti:sapphire oscillator. *Chinese Optics Letters* **2020**, *18*, 071402.
48. Liu, H.; Sun, S.; Zheng, L.; Wang, G.; Tian, W.; Zhang, D.; Han, H.; Zhu, J.; Wei, Z. Review of laser-diode pumped Ti:sapphire laser. *Microwave and Optical Technology Letters* **2021**, *63*, 2135–2144. https://doi.org/https://doi.org/10.1002/mop.32882.
49. Sugiyama, N.; Tanaka, H.; Kannari, F. Mode-locked Ti:sapphire laser oscillators pumped by wavelength-multiplexed laser diodes. *Japanese Journal of Applied Physics* **2018**, *57*, 052701. https://doi.org/10.7567/JJAP.57.052701.
50. Wang, Y.; Holguín-Lerma, J.A.; Vezzoli, M.; Guo, Y.; Tang, H.X. Photonic-circuit-integrated titanium:sapphire laser. *Nature Photonics* **2023**, *17*, 338–345. https://doi.org/10.1038/s41566-022-01144-2.